

See discussions, stats, and author profiles for this publication at: <https://www.researchgate.net/publication/260364725>

Amorphous Alumina Nanoparticles: Structure, Surface Energy, and Thermodynamic Phase Stability

ARTICLE in THE JOURNAL OF PHYSICAL CHEMISTRY C · AUGUST 2013

Impact Factor: 4.77 · DOI: 10.1021/jp405820g

CITATIONS

14

READS

98

8 AUTHORS, INCLUDING:



[Scarlett Widgeon](#)

University of California, Santa Barbara

17 PUBLICATIONS 140 CITATIONS

[SEE PROFILE](#)



[Jorgen Fredrick Rufner](#)

Intel

19 PUBLICATIONS 122 CITATIONS

[SEE PROFILE](#)



[Klaus van Benthem](#)

University of California, Davis

135 PUBLICATIONS 1,675 CITATIONS

[SEE PROFILE](#)



[Sergey V Ushakov](#)

University of California, Davis

69 PUBLICATIONS 1,040 CITATIONS

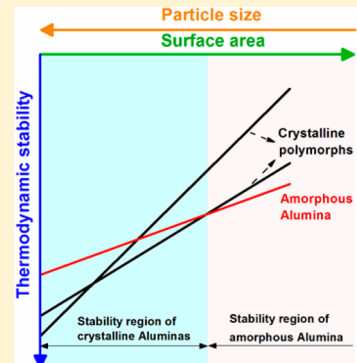
[SEE PROFILE](#)

Amorphous Alumina Nanoparticles: Structure, Surface Energy, and Thermodynamic Phase Stability

Amir H. Tavakoli,[†] Pardha Saradhi Maram,[†] Scarlett J. Widgeon,^{†,‡} Jorgen Rufner,^{†,‡} Klaus van Benthem,[‡] Sergey Ushakov,[†] Sabyasachi Sen,[‡] and Alexandra Navrotsky*,^{†,‡}

[†]Peter A. Rock Thermochemistry Laboratory and NEAT ORU and [‡]Department of Chemical Engineering and Materials Science, University of California, Davis, California 95616, United States

ABSTRACT: To provide a complete picture of the energy landscape of Al_2O_3 at the nanoscale, we directed this study toward understanding the energetics of amorphous alumina ($\text{a-Al}_2\text{O}_3$). $\text{a-Al}_2\text{O}_3$ nanoparticles were obtained by condensation from gas phase generated through laser evaporation of $\alpha\text{-Al}_2\text{O}_3$ targets in pure oxygen at 25 Pa. As-deposited nanopowders were heat-treated at different temperatures up to 600 °C to provide powders with surface areas of 670–340 m²/g. The structure of the samples was characterized by powder X-ray diffraction, transmission electron microscopy, and solid-state nuclear magnetic resonance spectroscopy. The results indicate that the microstructure consists of aggregated 3–5 nm nanoparticles that remain amorphous to temperatures as high as 600 °C. The structure consists of a network of AlO_4 , AlO_5 , and AlO_6 polyhedra, with AlO_5 being the most abundant species. The presence of water molecules on the surfaces was confirmed by mass spectrometry of the gases evolved on heating the samples under vacuum. A combination of BET surface-area measurements, water adsorption calorimetry, and high-temperature oxide melt solution calorimetry was employed for thermodynamic analysis. By linear fit of the measured excess enthalpy of the nanoparticles as a function of surface area, the surface energy of $\text{a-Al}_2\text{O}_3$ was determined to be $0.97 \pm 0.04 \text{ J/m}^2$. We conclude that the lower surface energy of $\text{a-Al}_2\text{O}_3$ compared with crystalline polymorphs γ - and $\alpha\text{-Al}_2\text{O}_3$ makes this phase the most energetically stable phase at surface areas greater than 370 m²/g.



1. INTRODUCTION

Amorphous alumina, $\text{a-Al}_2\text{O}_3$, is a multifunctional candidate material due to its electrical, optical, and catalytic properties as well as its oxidation and corrosion resistance.^{1–4} Particularly in microelectronic devices, use of $\text{a-Al}_2\text{O}_3$ films appears to be advantageous due to its low leakage current and high dielectric constant.^{4–7} Therefore, understanding the structure and energetics of $\text{a-Al}_2\text{O}_3$ can significantly contribute to the design and development of new materials and devices containing this phase. Because $\text{a-Al}_2\text{O}_3$ is expected to be used in practice as thin films and multilayers, understanding its surface/interface structure and energetics is of major fundamental and technological importance.

The bulk and surface thermodynamics of $\text{a-Al}_2\text{O}_3$ have not yet been experimentally investigated to the best of our knowledge. However, the structure of $\text{a-Al}_2\text{O}_3$ has been studied extensively, with major focus on probing the chemical environments of the Al and O ions using a variety of spectroscopic and computational techniques including solid-state nuclear magnetic resonance (NMR),^{8–10} X-ray photoelectron spectroscopy (XPS),¹¹ X-ray and neutron diffraction,^{12,13} extended X-ray absorption fine structure (EXAFS),¹⁴ molecular dynamic simulations,^{15–17} first-principles calculations of XPS and NMR spectra,¹⁸ and ab initio calculations.¹⁹ These investigations are overall in good agreement, indicating that the amorphous structure is composed of AlO_4 tetrahedra, AlO_5 polyhedra, and AlO_6 octahedra with predominant fractions of

AlO_4 and AlO_5 units. The simulations have shown that the relative ratios of polyhedra depend on the amorphous phase density.^{15,18} An Al coordination number of five has also been detected in liquid alumina,^{20,21} suggesting that the local structure in amorphous and liquid alumina may be similar; however, the existence of AlO_5 motifs has not been reported for any of the crystalline Al_2O_3 polymorphs. For instance, α - and $\gamma\text{-Al}_2\text{O}_3$ polymorphs contain AlO_6 and a mixture of AlO_6 and AlO_4 units, respectively. In addition to four-, five-, and six-coordinated Al ions, AlO_3 polyhedra can form in the top 0.3 nm layer of the $\text{a-Al}_2\text{O}_3$ surface according to surface structure simulations.¹⁷ The surface structure obviously contributes to the surface energetics and eventually can change the thermodynamic stability of materials at the nanoscale, as shown in the case of crystalline Al_2O_3 polymorphs. While bulk corundum, $\alpha\text{-Al}_2\text{O}_3$, is the thermodynamically stable bulk phase, a lower surface energy of $\gamma\text{-Al}_2\text{O}_3$ ($\gamma_s = 1.5$ to 1.7 J/m^2)^{22–24} than $\alpha\text{-Al}_2\text{O}_3$ ($\gamma_s = 2.64 \text{ J/m}^2$)²² makes the former energetically stable at surface areas greater than $\sim 125 \text{ m}^2/\text{g}$. Likewise, the stabilization induced by lower surface energy of one polymorph over another has been demonstrated for nanocrystalline ZrO_2 ,²⁵ TiO_2 ,²⁶ Fe_2O_3 ,²⁷ and HfO_2 .²⁸ Moreover, the thermodynamic phase stability of the amorphous

Received: June 12, 2013

Revised: July 18, 2013

Published: July 22, 2013

nanoparticles with respect to the nanocrystalline polymorphs has been previously reported for zirconia.²⁵

In the present study, we investigate the possible thermodynamic stability of α -Al₂O₃ nanoparticles relative to γ - and α -Al₂O₃ by the determination of the surface energy and bulk excess enthalpy of α -Al₂O₃ through calorimetric measurements on fully characterized amorphous nanoparticles. The outcome of this work enables us to complete the thermodynamic phase stability diagram of Al₂O₃ at the nanoscale initially established for the crystalline polymorphs γ - and α -Al₂O₃.²²

2. EXPERIMENTAL PROCEDURES

2.1. Materials and Methods. α -Al₂O₃ nanoparticles were obtained using a custom-made gas-phase condensation setup designed for laser evaporation of a solid target in a controlled atmosphere synthesis chamber. (See ref 29 for details.) The Al₂O₃ targets for evaporation were prepared by cutting dense alumina discs (Coorstek, 99.8%) into small cuboids (15 × 15 × 6 mm). Prior to vaporization, the synthesis chamber was evacuated below 1 Pa using an oil-free scroll pump and then filled to ~25 Pa with 99.9% oxygen gas. The CW-CO₂ laser beam, focused on the target rotating at 6 rpm, was set at the operating power of 40 W throughout the evaporation time of ~1 h. Nanoparticles formed on condensation were collected on a stainless-steel shim located at a 50 mm distance from the target. After synthesis, the entire chamber was transferred to a N₂-filled glovebox to minimize water uptake of the hydrophilic deposits. The as-deposited powders were scraped off the steel shim and stored inside the glovebox for measurements. Annealing of the as-deposited powders at different temperatures up to 1350 °C was carried out in Pt crucibles using a Netzsch 404 DSC instrument installed in the glovebox.

2.2. Characterization. X-ray diffraction (XRD) patterns were collected using a Bruker AXS D8 Advance diffractometer applying Cu K α radiation (40 kV/40 mA). Prior to the XRD analysis, the alumina powders were transferred to an airtight sample holder inside the glovebox.

The morphology of alumina particles was determined by transmission electron microscopy (TEM) using a JEOL JEM-2500SE transmission electron microscope operated at 200 kV. Particle size distributions were analyzed from bright-field TEM images with no additional image processing. For sample preparation, the particles were dispersed in ethanol and subsequently drop-casted on holey carbon films supported by TEM specimen grids. To confirm lack of crystallinity of the as-deposited and annealed samples, we performed selected area electron diffraction (SAED) with particles reaching over holes of the support film to avoid electron diffraction intensities from the amorphous carbon.

Surface area was measured using a Micromeritics ASAP 2020 instrument applying the Brunauer–Emmett–Teller (BET) method. Five-point adsorption isotherms of nitrogen at −196 °C were collected in the P/P° relative pressure range from 0.05 to 0.3, where P° is the saturation pressure at −196 °C. In addition, full nitrogen adsorption/desorption isotherm ($P/P^{\circ} = 1$) experiments were carried out after degassing of the as-deposited alumina and annealed sample at elevated temperatures to keep track of the change in interparticle void space and size when the surface area is diminished on annealing.

²⁷Al magic-angle-spining (MAS) and triple-quantum (3Q) MAS NMR spectra of the as-deposited and annealed alumina samples were obtained using a Bruker Avance solid-state spectrometer operating at a Larmor frequency of 130.3 MHz

for ²⁷Al. Nanopowder samples were packed in zirconia rotors under a nitrogen atmosphere and spun at 20 kHz using a 2.5 mm Bruker CPMAS probe. ²⁷Al chemical shifts were externally referenced to 1 M aqueous solution of Al(NO₃)₃. ²⁷Al one-pulse MAS spectra were collected using a $\pi/6$ (0.3 μ s) rf pulses and 0.2 s recycle delay. Approximately 120 free induction decays (FIDs) were averaged and Fourier-transformed to obtain each ²⁷Al MAS NMR spectrum. ²⁷Al 3QMAS NMR spectra of the alumina samples were obtained using a three-pulse zero quantum filtered pulse program. The high power excitation and conversion pulse lengths were optimized to 4.0 and 1.4 μ s, respectively, and the length of the $\pi/2$ selective pulse was 46.8 μ s. A series of 64 t_1 slices were collected using 1248 FIDs with a recycle delay of 0.7 s for each slice. A half rotor cycle of 25.0 μ s was used as the time increment between slices. The ²⁷Al 3QMAS spectra were processed using the Bruker Topspin software.

To check the potential surface occupation by adsorbents such as H₂O and CO₂, pellets made of the as-deposited nanopowders were placed into a silica glass tube inside the glovebox, then transferred out, evacuated to 10^{−3} Pa s, and heated to 900 °C using a small vertical tube furnace. Analysis of evolved gases was performed using a Pfeiffer PrismaPlus QMG 220 mass spectrometer.

2.3. Calorimetry. High-temperature oxide melt solution calorimetry was done using a Tian-Calvet twin calorimeter described in detail elsewhere.^{30,31} Sample preparation was done inside the N₂-filled glovebox. For each experiment, a ~5 mg pellet, made by pressing powders in a 3 mm die, was sealed in a capped vial, then transferred from the glovebox to the calorimetry room, and finally dropped into the solvent (molten 2PbO·B₂O₃ at 703 °C) in a platinum crucible in the calorimeter, right after opening the sealed vial. Total exposure to air was <2 s. In each experiment, the calorimetric signal collected represents the sum of heat content of the sample from room temperature to 703 °C, heat of desorption of gas molecules, and heat of solution of the sample in the solvent. Multiple runs of ~5 mg pellets were conducted to obtain appropriate statistics. The calorimetry assembly was continuously flushed with dry air at 80 mL/min to prevent sample exposure to water vapor and to remove the evolved gases. Calibration was performed by dropping α -Al₂O₃ pellets into an empty platinum crucible. The calorimetric protocol is well-established, and no special problems were encountered.

The enthalpy of water vapor adsorption was measured at 25 °C using a Setaram Sensys Calvet calorimeter coupled to a Micromeritics ASAP 2020. This system enables precise gas dosing, volumetric detection of the amount of adsorbed water, and simultaneous measurement of the heat effect. Instrumentation and analysis procedure are described in detail elsewhere.^{32,33} Prior to gas adsorption experiments, samples were degassed at 600 °C for 30 min under continuous dynamic vacuum to remove the pre-existing adsorbed H₂O. The total surface area of the samples was 4–6 m², and the dose amount of H₂O vapor was set at 1 μ mol/m². The calorimeter was calibrated against the enthalpy of fusion of gallium metal.

3. RESULTS

3.1. Structure. The X-ray diffraction pattern of the as-deposited powders is presented in Figure 1. Absence of peaks corresponding to distinct crystalline polymorphs of Al₂O₃ confirms the amorphous nature of the obtained material. Because systematic calorimetric measurements of nanoscale

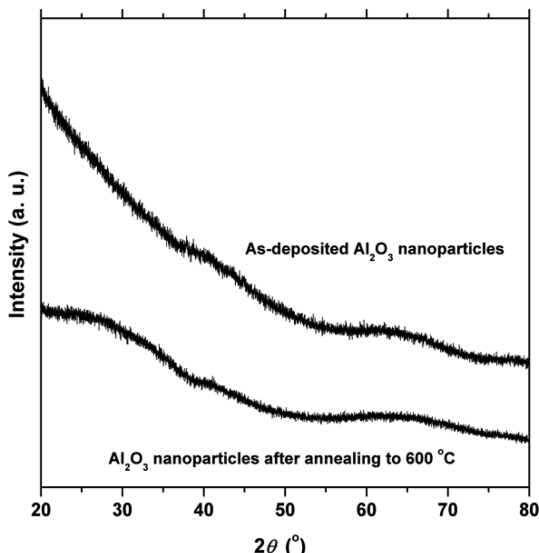


Figure 1. X-ray diffraction (XRD) spectra of the as-deposited and heat-treated amorphous alumina ($\text{a-Al}_2\text{O}_3$) powders.

materials require a series of samples with varying surface area, the as-deposited $\text{a-Al}_2\text{O}_3$ nanoparticles were heat-treated at three different temperatures (200, 300, and 600 °C) to diminish the surface area. The low annealing temperatures were chosen to avoid crystallization. The XRD profile of the sample annealed at 600 °C indicates that the material has not crystallized. (See Figure 1.) TEM and NMR characterizations were conducted on the as-deposited sample and the sample annealed at 600 °C to probe the change in the microstructure and local structure upon heating. The TEM images, shown in Figure 2, were recorded with relatively large defocus (± 200 –300 nm) to improve contrast. For both samples, agglomeration

made the identification of individual nanoparticles difficult. Nevertheless, the average particle sizes were carefully determined by calculating dimensions of 50 grains randomly selected from the TEM micrographs of each sample. While the average particle sizes of 3.6 ± 0.4 nm were obtained for the as-deposited alumina nanoparticles, the nanoparticles annealed at 600 °C are slightly larger around 4.8 ± 0.5 nm. Selected area electron diffraction (SAED) patterns shown in the inset of Figure 2a,c reveal an amorphous structure before and after annealing, in accord with the results of XRD. The ^{27}Al MAS NMR spectra of the as-deposited nanopowders and the annealed alumina at 600 °C show three resonances located at approximately 71, 40, and 7 ppm that correspond to four-, five-, and six-coordinated Al. (See Figure 3a.) Because of the overlapping signals in the MAS NMR spectra, we collected ^{27}Al 3QMAS NMR spectra to obtain higher resolution of the various Al sites. These spectra, shown in Figure 3a,b, verify the presence of the three distinct sites in both samples, where the isotopic chemical shift, δ_{iso} , of the four-, five-, and six-coordinated sites is, respectively, at 70 (71), 41 (40), and 9 ppm (10 ppm) for the as-deposited (annealed) sample. The quadrupolar coupling constants, C_Q , calculated for the available sites, were found to be 4.9 (4.7), 4.8 (4.6), and 3.5 MHz (3.3 MHz). These values are typical of the C_Q values found in previous studies of alumina materials with similar bonding environments.³⁴ The isotropic projections of these ^{27}Al 3QMAS NMR spectra, although not fully quantitative by themselves, are expected to yield quantitative comparisons of the relative fractions of various Al sites between the two samples. Simulations of these isotropic projections with Gaussian line shapes yield relative fractions ($\pm 4\%$) of 19 (27), 67 (54), and 14 (19) % for four-, five-, and six-coordinated Al ions in the as-deposited (annealed) samples. Therefore, annealing of the $\text{a-Al}_2\text{O}_3$ nanoparticles results in a decrease in five-coordinated Al at the expense of the four- and six-coordinated species.

3.2. Surface Energy. Prior to calorimetric measurements, the surface-adsorbed species and surface area of $\text{a-Al}_2\text{O}_3$ nanoparticles must be quantified. Despite using pure oxygen for evaporation and low H_2O pressure in the glovebox (-79 °C dew point), mass loss of the nanopowders as a function of annealing temperature up to 1350 °C was detected by weighing the pelletized nanopowders inside the glovebox, indicating that gaseous species are evolved upon increasing temperature. The analysis of desorbed gases as a function of temperature by mass spectrometry reveals loss of water vapor as the only desorbing gas at the temperatures above 100 and below 800 °C. Above 800 °C, in addition to water vapor, the mass spectra show evolution of N_2 gas with a much lower intensity than water vapor, indicating minor surface adsorption of N_2 from the glovebox. Because the mass loss above 800 °C was found to be negligible and within the uncertainty limit, mass spectrometry confirms that H_2O is the only major component absorbed on the surface. We conclude that these $\text{a-Al}_2\text{O}_3$ samples are very efficient at getting traces of water in the synthesis chamber or in the glovebox. The total water loss after annealing in the glovebox was 8.5 ± 0.2 wt.%, while equilibration of the as-deposited $\text{a-Al}_2\text{O}_3$ at 50% humidity resulted in ~40% mass loss after heating (about five times more than the measured mass loss in the glovebox). This indicates that the obtained nanopowders are only partially hydrated. The compositions of samples ($\text{a-Al}_2\text{O}_3 \cdot n\text{H}_2\text{O}$) made at different annealing temperatures in the glovebox are listed in Table 1. It is notable

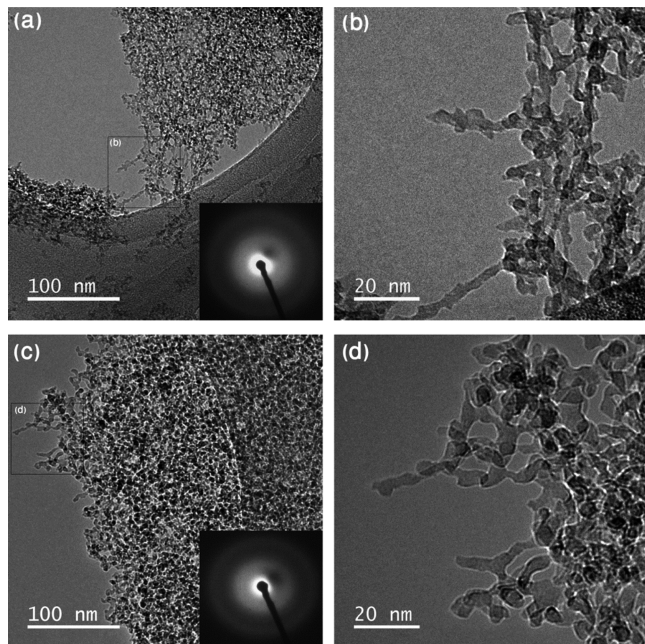


Figure 2. TEM micrographs of the $\text{a-Al}_2\text{O}_3$ samples: (a,b) as-deposited powders and (c,d) annealed powders at 600 °C. Selected area diffraction patterns of the samples are shown in the inset of panels a and c.

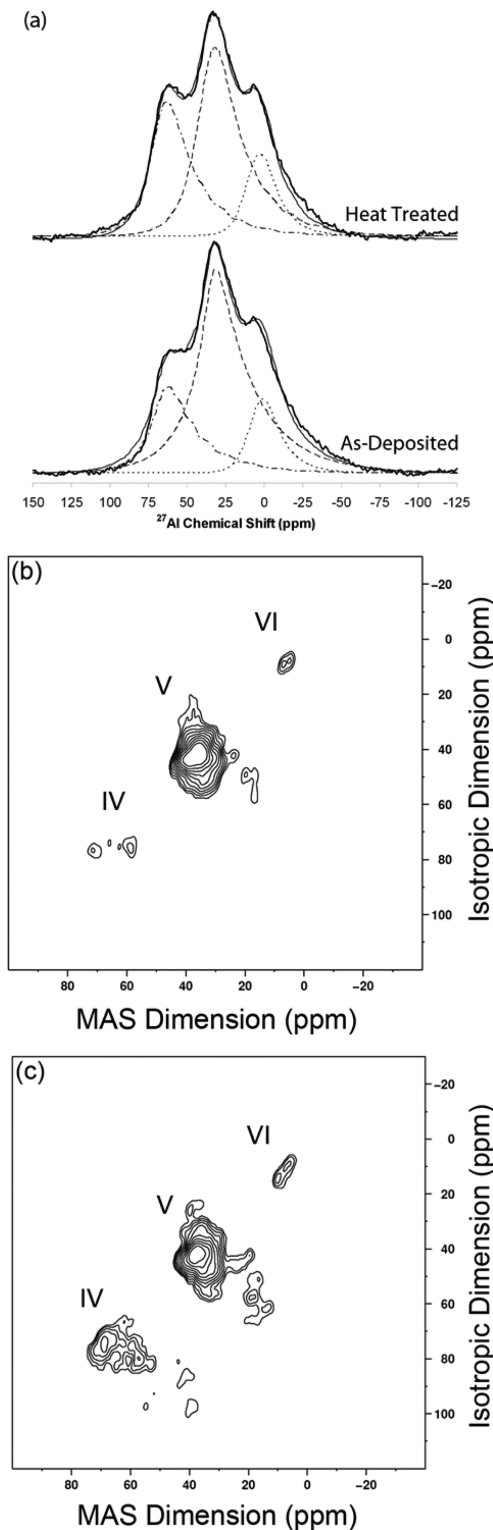


Figure 3. (a) ²⁷Al MAS NMR spectra of the as-deposited and heat-treated ($600\text{ }^{\circ}\text{C}$) $\text{a-Al}_2\text{O}_3$ samples. The deconvoluted signals are resonances corresponding to four-, five-, and six-coordinated Al, respectively, from left to right. (b,c) ²⁷Al 3QMAS NMR spectra of the as-deposited $\text{a-Al}_2\text{O}_3$ nanopowders and annealed sample at $600\text{ }^{\circ}\text{C}$, respectively.

that while the mass spectrometry results show water loss starting above $100\text{ }^{\circ}\text{C}$, no water loss was detected by weighing the pelletized nanopowders before and after annealing to $200\text{ }^{\circ}\text{C}$ in the glovebox. This different behavior is attributed to

different equilibrium conditions for desorption of water molecules because of the tremendously different applied N_2 partial pressure. (The mass spectrometry was done at $\sim 10^{-3}$ Pa, while annealing of the samples was done in the glovebox filled with N_2 at a pressure slightly above 10^5 Pa.) The BET surface areas (SAs) measured for the as-deposited sample and annealed samples at 200 , 300 , and $600\text{ }^{\circ}\text{C}$ are given in Table 1. The initial SA of $670.6 \pm 6.5\text{ m}^2/\text{g}$ measured for the as-deposited sample diminishes to $336.7 \pm 12.1\text{ m}^2/\text{g}$ upon increasing the annealing temperature to $600\text{ }^{\circ}\text{C}$.

The drop-solution enthalpies, ΔH_{ds} , of the studied samples are given in Table 1. As previously explained, the samples investigated in this study appear to be partially hydrated, so the energy of fully hydrated surfaces is not a well-defined quantity in this study. Thus we concentrate on the determination of the energy of anhydrous $\text{a-Al}_2\text{O}_3$ surfaces, for which it is essential to correct the ΔH_{ds} values for the adsorption enthalpy of water caused by the bonding of H_2O to the surface. The enthalpy of condensation of water at $25\text{ }^{\circ}\text{C}$, namely, its physisorption enthalpy, is -44 kJ/mol . When the enthalpy of water adsorption is more negative than -44 kJ/mol , the adsorption is regarded as chemisorption. The results of water adsorption calorimetry on $\text{a-Al}_2\text{O}_3$ are shown in Figure 4. The first dose of water vapor at $\sim 1\text{ }\mu\text{mol H}_2\text{O/m}^2$ gives a strongly negative heat of adsorption (-106 kJ/mol). The heat of adsorption becomes less exothermic with increasing H_2O coverage and reaches -44 kJ/mol at a coverage of $9.8\text{ H}_2\text{O/nm}^2$, indicating physisorption of water at higher coverage. By summing the enthalpies of adsorption for all doses and dividing by the total number of moles of adsorbed water up to the coverage given above, the integral enthalpy of adsorption for chemisorbed water, ΔH_{ads} , is obtained to be $-63.9 \pm 1.5\text{ kJ/mol}$. According to the measured total water content of the as-deposited amorphous nanoparticles (8.5 wt \%), the water coverage was calculated to be $4.17\text{ H}_2\text{O/nm}^2$, which is almost two times smaller than the total coverage of chemisorbed water ($9.79\text{ H}_2\text{O/nm}^2$), confirming that our nanopowders for oxide-melt solution calorimetry are only partially hydrated. (The goal was to make the nanopowders completely anhydrous, but this proved unfeasible.) Therefore, the obtained ΔH_{ds} values were corrected only for the enthalpy of adsorption of the measured amount of chemisorbed water using the thermodynamic cycle presented in Table 2a. The obtained enthalpies, $\Delta H_{ds,\text{corrected}}$, listed in Table 1 represent the drop-solution enthalpies of $\text{a-Al}_2\text{O}_3$ nanoparticles with anhydrous surfaces. By subtracting the $\Delta H_{ds,\text{corrected}}$ values from the drop-solution enthalpy of bulk corundum ($\alpha\text{-Al}_2\text{O}_3$), as shown in Table 2b, the excess enthalpies of anhydrous $\text{a-Al}_2\text{O}_3$ nanoparticles with respect to the most thermodynamically stable bulk Al_2O_3 polymorph (corundum), ΔH^{xs} , are obtained (Table 1 and Figure 5). The linear fit to the ΔH^{xs} –SA data in Figure 5 yields the equation

$$\Delta H^{xs}(\text{J/mol}) = (0.97 \pm 0.04) \cdot (\text{SA}) + (39305.25 \pm 2353.44); R^2 = 0.994 \quad (1)$$

The slope and intercept of the fitted line represent, respectively, the surface energy of $\text{a-Al}_2\text{O}_3$, γ_s , equal to $0.97 \pm 0.04\text{ J/m}^2$, and the enthalpy of the $\alpha \rightarrow \text{a}$ transition in bulk Al_2O_3 , $\Delta H_{\alpha \rightarrow \text{a}} = 39305 \pm 2353\text{ J/mol}$.

Table 1. Annealing Temperatures, Compositions, Surface Areas, and Drop-Solution Enthalpies (ΔH_{ds}) of $\alpha\text{-Al}_2\text{O}_3$ Nanoparticles in Addition to the Corrected ΔH_{ds} Values for Chemisorbed Water ($\Delta H_{ds\text{-corrected}}$) and the Corresponding Excess Enthalpies Relative to $\alpha\text{-Al}_2\text{O}_3$, Corundum (ΔH^{xs})

annealing temperature (°C)	composition	surface area (SA) (m ² /g, m ² /mol) ^a	ΔH_{ds} (kJ/mol)	$\Delta H_{ds\text{-corrected}}$ (kJ/mol) ^b	ΔH^{xs} (kJ/mol) ^c
not annealed	$\text{Al}_2\text{O}_3\text{:}0.52\text{H}_2\text{O}$	$670.6 \pm 6.5, 74651 \pm 724$	$39.7 \pm 1.2 (6)^d$	-6.5 ± 1.6	112.8 ± 1.7
200	$\text{Al}_2\text{O}_3\text{:}0.52\text{H}_2\text{O}$	$591.3 \pm 19.7, 65823 \pm 2188$	$51.6 \pm 1.4 (6)$	5.4 ± 1.8	100.9 ± 1.9
300	$\text{Al}_2\text{O}_3\text{:}0.38\text{H}_2\text{O}$	$459.1 \pm 3.2, 49950 \pm 346$	$52.4 \pm 0.8 (6)$	18.6 ± 1.1	87.7 ± 1.2
600	$\text{Al}_2\text{O}_3\text{:}0.25\text{H}_2\text{O}$	$336.7 \pm 12.1, 35825 \pm 1286$	$54.4 \pm 0.9 (6)$	32.2 ± 1.0	74.1 ± 1.1

^aObtained by averaging the surface area measured for two different batches of each composition. ^bCalculated using the thermodynamic cycle given in Table 2a. ^cCalculated using the thermodynamic cycle given in Table 2b. ^dNumbers in parentheses represent number of measurements.

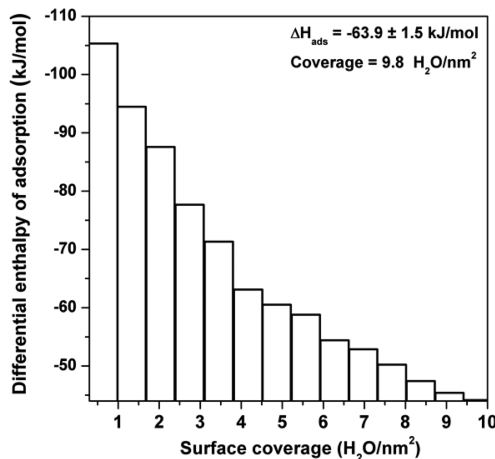


Figure 4. Differential enthalpy of water adsorption as a function of water coverage for the as-deposited $\text{a-Al}_2\text{O}_3$ nanoparticles degassed at 600 °C. Each column bar at a given coverage was obtained by averaging test results from two different batches.

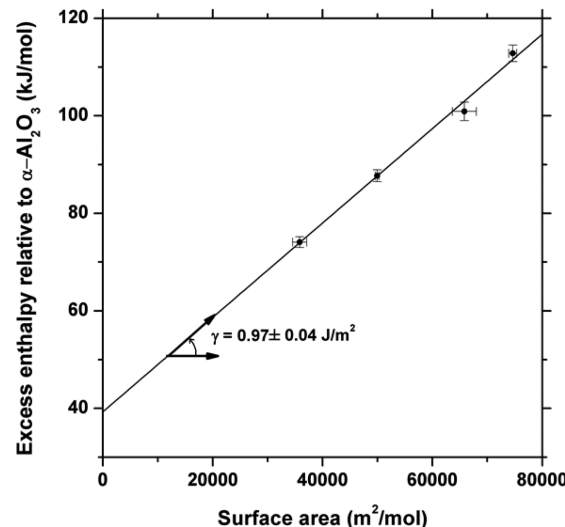


Figure 5. Excess enthalpy of $\text{a-Al}_2\text{O}_3$ nanoparticles, ΔH^{xs} , as a function of surface area, SA. Slope and intercept of the fitted line to the data provide, respectively, the specific surface energy of $\text{a-Al}_2\text{O}_3$, γ_s , and the excess enthalpy of bulk $\text{a-Al}_2\text{O}_3$ with respect to $\alpha\text{-Al}_2\text{O}_3$.

4. DISCUSSION

The N₂ adsorption/desorption isotherms performed on the $\text{a-Al}_2\text{O}_3$ samples showed pronounced desorption hysteresis, suggesting the existence of mesopores (~2.7 nm) in interparticle spaces. The data analysis indicates that the total pore volume diminishes from 0.42 to 0.23 cm³/g with increasing temperature to 600 °C. This finding can be attributed to the formation of solid–solid interfaces during annealing. TEM images in Figure 2 show these solid–solid interfaces as interparticle necking between some nanoparticles, giving rise to the formation of chain-like structures. Therefore, we conclude that the decrease in surface area by increase in the

heat treatment-temperature (see Table 1) is due to both coarsening of the nanoparticles, as shown in the TEM images, and the formation of amorphous solid/solid interfaces. As shown in previous works,^{35,36} the interface enthalpy arising from such grain–grain contacts can contribute to the excess enthalpy of nanoparticles, ΔH^{xs} . Thus, ΔH^{xs} can be expressed as

$$\Delta H^{xs} = \gamma_s \cdot (\text{SA}) + \Delta H_{\alpha \rightarrow a} + \gamma_i \cdot (\text{IA}) \quad (2)$$

where γ_i is the solid/solid interface energy and IA is the interface area. Despite the plausible formation of interfaces in

Table 2. Thermodynamic Cycles for (a) Correcting the Enthalpies of Drop-Solutions of $\text{a-Al}_2\text{O}_3$ Nanoparticles for Chemisorbed Water, $\Delta H_{ds\text{-corrected}}$, and (b) Calculating the Excess Enthalpies of $\text{a-Al}_2\text{O}_3$ Nanoparticles Relative to Bulk Corundum, ΔH^{xs}

reaction	enthalpy (kJ/mol)
(a) Drop-Solution Enthalpies of $\text{a-Al}_2\text{O}_3$ Corrected for Chemisorbed Water ($\Delta H_{ds\text{-corrected}}$)	
(1) $\text{a-Al}_2\text{O}_3\text{:}x\text{H}_2\text{O}$ (nanoparticles, 25 °C) = Al_2O_3 (dissolved, 703 °C) + $x\text{H}_2\text{O}$ (g, 703 °C)	$\Delta H_1 = \Delta H_{ds}$
(2) $\text{a-Al}_2\text{O}_3$ (nanoparticles, 25 °C) + H_2O (g, 25 °C) = $\text{a-Al}_2\text{O}_3\text{:H}_2\text{O}$ (nanoparticles, 25 °C)	$\Delta H_2 = \Delta H_{ads} = -63.9 \pm 0.5$
(3) H_2O (g, 25 °C) = H_2O (g, 703 °C)	$\Delta H_3 = 25.0 \pm 0.5$ ³⁹
(4) $\text{a-Al}_2\text{O}_3$ (nanoparticles, 25 °C) = Al_2O_3 (dissolved, 703 °C)	$\Delta H_4 = \Delta H_{ds\text{-corrected}}$
$\Delta H_4 = \Delta H_1 + x \cdot \Delta H_2 - x \cdot \Delta H_3$	
(b) Excess Enthalpies of $\text{a-Al}_2\text{O}_3$ Relative to Bulk Corundum (ΔH^{xs})	
(5) $\text{a-Al}_2\text{O}_3$ (nanoparticles, 25 °C) = Al_2O_3 (dissolved, 703 °C)	$\Delta H_5 = \Delta H_4$
(6) Al_2O_3 (corundum, 25 °C) = Al_2O_3 (dissolved, 703 °C)	$\Delta H_6 = 106.4 \pm 0.5$ ²²
(7) Al_2O_3 (corundum, 25 °C) = $\text{a-Al}_2\text{O}_3$ (nanoparticles, 25 °C)	$\Delta H_7 = \Delta H^{xs}$
$\Delta H_7 = \Delta H_5 - \Delta H_6$	

the a-Al₂O₃ samples, the linear regression of the ΔH_{xs} values as a function of SA yielded $R^2 = 0.994$ (see Figure 5), confirming that there is a linear correlation between the excess enthalpy, ΔH_{xs} , and surface area SA of a-Al₂O₃. The lack of curvature in the plot suggests that the effect of the interface enthalpy term in eq 2 is very small and may be negligible. To provide an estimate of the magnitude of γ_1 (IA), we consider the sample annealed at 600 °C with the greatest IA of about 83.1 m²/g (IA ≈ ((SA₀ · ⟨d₀⟩/⟨d⟩) − (SA))/2) ≈ (670.6 · (3.6/4.8) − 336.7/2), where SA₀ and ⟨d₀⟩ are constants equal to the surface area and average particle size of the as deposited am-Al₂O₃) and the smallest measured SA of 336.7 m²/g among the samples studied in this work. Taking the calorimetrically measured amorphous/crystalline interface energy, 0.3 J/m²^{28,37} as the upper limit of γ_1 and $\gamma_s = 0.97$ J/m² as obtained in this work, γ_1 (IA) ≈ 2.5 kJ/mol and γ_s (SA) ≈ 33.3 kJ/mol are calculated. This reveals that the surface enthalpy contribution is more than 13 times larger than the interface enthalpy contribution for the a-Al₂O₃ sample with maximal IA and minimal SA. This estimation justifies neglecting the interface enthalpy contribution compared with the surface enthalpy term.

The calorimetrically obtained surface enthalpy of a-Al₂O₃ determined in this work ($\gamma_s = 0.97 \pm 0.04$ J/m²) agrees well with the only available data in the literature, a theoretically calculated surface energy based on molecular dynamics simulations of the a-Al₂O₃ surface structure ($\gamma_s = 0.88$ J/m²).¹⁷ The fitted line to the ΔH^{xs} data of a-Al₂O₃ nanoparticles presented in Figure 5 and the previously derived linear equations representing the ΔH^{xs} data as a function of SA for

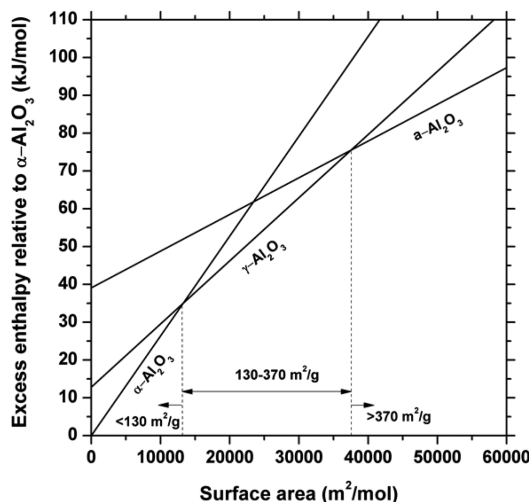


Figure 6. Derived linear functions, representing excess enthalpies of a-Al₂O₃^{this work} γ -Al₂O₃, and α -Al₂O₃²² nanoparticles as a function of surface area. The excess enthalpy of a-Al₂O₃ lies lower than that of γ -Al₂O₃ at the given surface area, 370 m²/g, demonstrating that a-Al₂O₃ is the most energetically stable phase when specific surface area exceeds 370 m²/g. The stability region of γ -Al₂O₃ is at the surface areas between 130 and 370 m²/g, below which α -Al₂O₃ shows the greatest stability.

γ - and α -Al₂O₃ nanoparticles²² are plotted together in Figure 6. In this Figure, the excess enthalpy line of a-Al₂O₃ lies lower than that of γ -Al₂O₃ at surface areas over 370 m²/g because a-Al₂O₃ has a considerably lower surface energy than γ -Al₂O₃ ($\gamma_{s,\gamma\text{-Al}_2\text{O}_3} = 1.5$ to 1.7 J/m²)^{22–24}. This means that a-Al₂O₃ nanoparticles become energetically more stable than γ -Al₂O₃

when the specific surface area exceeds 370 m²/g. In other words, the enthalpic stability of γ -Al₂O₃ nanoparticles is limited to surface areas ranging from ~130 to 370 m²/g, below which α -Al₂O₃ becomes the most stable phase. The lower surface energy of a-Al₂O₃ compared with that of the crystalline polymorphs is suggested to be, at least in part, due to the dominant surface occupation of AlO₅ polyhedra, which is unique to the amorphous state. The diminished fraction of five-coordinated Al with decrease in surface area, as shown in Figure 3, suggests energetically favorable surface occupancy of AlO₅ units.

Using the excess enthalpy trend lines in Figure 6, the transition enthalpies of a-Al₂O₃ to crystalline polymorphs γ - and α -Al₂O₃ ($\Delta H_{t(a \rightarrow \gamma)}$ and $\Delta H_{t(a \rightarrow \alpha)}$) and that of γ - to α -Al₂O₃ ($\Delta H_{t(\gamma \rightarrow \alpha)}$) were calculated by subtracting the ΔH^{xs} values of the relevant phases at constant surface areas. The obtained data

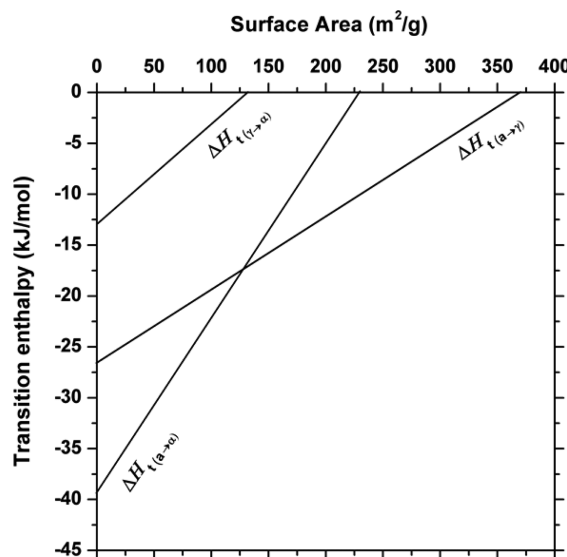


Figure 7. Transition enthalpies of a \rightarrow γ -Al₂O₃, $\Delta H_{t(a \rightarrow \gamma)}$; a \rightarrow α -Al₂O₃, $\Delta H_{t(a \rightarrow \alpha)}$; and γ \rightarrow α -Al₂O₃, $\Delta H_{t(\gamma \rightarrow \alpha)}$ at bulk and nanoscale.

as a function of SA are plotted in Figure 7, showing how the transition enthalpies vary at the nanoscale: the greater the surface area, the smaller the transition enthalpies. Furthermore, this Figure demonstrates that the favorable energetic pathway for the a- to α -Al₂O₃ phase transition goes through the formation of γ -Al₂O₃ or the other likely transitional aluminas, as usually observed in experiments. The measured energetics in Figure 7 can be compared with several other experimental observations. For example, DSC on thick films (2.3–82 μ m) shows that the transition enthalpies of bulk a- to nanocrystalline bulk γ -Al₂O₃ and that of nanocrystalline bulk γ -Al₂O₃ to bulk α -Al₂O₃ alumina are -25.4 ± 7.5 and -13.0 ± 1.3 kJ/mol.³⁸ The transition enthalpies of a- to γ -Al₂O₃ and γ - to α -Al₂O₃ at SA = 0 in Figure 7 are -26.5 and -12.8 kJ/mol, indicating very good agreement with the DSC data obtained independently on different materials. Another example can be the comparison of the amorphization and fusion enthalpies. The transition enthalpy of α - to a-Al₂O₃ at room temperature, 39.3 kJ/mol (see Figure 7), is almost three times smaller than the fusion enthalpy of α -Al₂O₃ at 2054 °C, 111.1 \pm 4.2 kJ/mol.³⁹ If the amorphous phase represents a glass-like structural state derived from the supercooled liquid, separated by some intervening glass transition, then this difference is of reasonable magnitude.

The free energies of transition will be somewhat different from the enthalpies, even if there are no excess surface entropy terms. This difference arises mainly from distinct configurational entropies of Al_2O_3 phases. $\alpha\text{-Al}_2\text{O}_3$ is an ordered structure and therefore has configurational entropy of zero. However, both γ - and $\alpha\text{-Al}_2\text{O}_3$ have disorder leading to some configurational entropy. $\alpha\text{-Al}_2\text{O}_3$ is obviously more disordered than $\gamma\text{-Al}_2\text{O}_3$ due to the lack of crystallinity and a greater concentration of defects and polyhedra containing Al in four-, five-, and six-fold coordination in its structure. Thus, the positive entropy change in the α - to $\gamma\text{-Al}_2\text{O}_3$ transition, $\Delta S_{\alpha \rightarrow \gamma}$, can be assumed to be smaller than that in the α - to $\alpha\text{-Al}_2\text{O}_3$ transition, $\Delta S_{\alpha \rightarrow \alpha}$. At room temperature, the $T\Delta S$ terms are small and the enthalpies remain the leading term in the excess Gibbs free energy of γ - and $\alpha\text{-Al}_2\text{O}_3$ relative to $\alpha\text{-Al}_2\text{O}_3$, $\Delta G^{\text{ex}} = \Delta H^{\text{ex}} - T\Delta S$. Nevertheless, the greater configurational entropy of $\alpha\text{-Al}_2\text{O}_3$ compared with $\gamma\text{-Al}_2\text{O}_3$ causes the Gibbs free energy crossovers to occur at a smaller surface area compared with the enthalpy crossovers shown in Figure 6. In other words, $\alpha\text{-Al}_2\text{O}_3$ becomes thermodynamically more stable than $\gamma\text{-Al}_2\text{O}_3$ at a surface area slightly smaller than $370 \text{ m}^2/\text{g}$, which was measured based on the excess enthalpy data at room temperature. Considering a spherical shape for nanoparticles and the bulk density of $\alpha\text{-Al}_2\text{O}_3$ of 2.5 g/cm^3 , as approximated for the as-deposited $\alpha\text{-Al}_2\text{O}_3$ sample ($\rho \approx 6/(SA_0 \cdot \langle d \rangle)$), the surface area of $370 \text{ m}^2/\text{g}$ corresponds to an average particle size of $\sim 6.5 \text{ nm}$ ($\langle d \rangle \approx 6/(\rho \cdot SA)$). Therefore, $\alpha\text{-Al}_2\text{O}_3$ nanoparticles are expected to remain energetically stable at particle sizes smaller than 6.5 nm . Interestingly, in accord with this conclusion, it is shown in the literature that the $2\text{--}6 \text{ nm}$ thick $\alpha\text{-Al}_2\text{O}_3$ layers in yttria-stabilized zirconia (YSZ)/ Al_2O_3 remain amorphous when heated to 1000°C , while the 20 nm thick $\alpha\text{-Al}_2\text{O}_3$ layers crystallize to $\gamma\text{-Al}_2\text{O}_3$ when heated above 900°C .^{38,40} Although the YSZ/ Al_2O_3 interface enthalpy may also contribute to the stabilization of the amorphous phase, this example appears at least qualitatively consistent with the thermochemical data obtained in the present study. Thus the fundamental and technological use of the energy crossovers and transition enthalpies at the nanoscale (Figures 6 and 7) is not limited to Al_2O_3 nanoparticles but can also be applied to thin films and multilayers.

5. CONCLUDING REMARKS

The gas-phase synthesis of 3 to 4 nm $\alpha\text{-Al}_2\text{O}_3$ enabled us to analyze the structure, surface chemistry and surface energetics of the materials. The NMR analysis confirms that five-coordinated Al is the predominant Al-O polyhedral motif in the structure. The surface energy was determined to be $0.97 \pm 0.04 \text{ J/m}^2$ by calorimetric measurements. While bulk $\alpha\text{-Al}_2\text{O}_3$ is a metastable phase with respect to coarse $\gamma\text{-Al}_2\text{O}_3$ and $\alpha\text{-Al}_2\text{O}_3$, it gains excess enthalpy more gradually than the crystalline polymorphs with increasing surface area because of its lower surface energy and becomes energetically the most stable phase at surface areas greater than $370 \text{ m}^2/\text{g}$.

AUTHOR INFORMATION

Corresponding Author

*E-mail: anavrotsky@ucdavis.edu. Tel: (530) 752 3292.

Notes

The authors declare no competing financial interest.

ACKNOWLEDGMENTS

The synthesis and calorimetry were supported by the U.S. Department of Energy, grant DE-FG02-05ER115667. The TEM work was funded by University of California Laboratory Fee grant #12-LR-238313. The solid-state NMR spectroscopy was supported by a grant from the National Science Foundation (NSF GOALI1104869).

REFERENCES

- (1) Samelor, D.; Lazar, A. M.; Aufray, M.; Tendero, C.; Lacroix, L.; Beguin, J. D.; Caussat, B.; Vergnes, H.; Alexis, J.; Poquillon, D.; et al. Amorphous Alumina Coatings: Processing, Structure and Remarkable Barrier Properties. *J. Nanosci. Nanotechnol.* **2011**, *11*, 8387–8391.
- (2) Khan, G. G.; Singh, A. K.; Mandal, K. Structure Dependent Photoluminescence of Nanoporous Amorphous Anodic Aluminium Oxide Membranes: Role of F+ Center Defects. *J. Lumin.* **2013**, *134*, 772–777.
- (3) de Castro, M. J.; Serna, R.; Chaos, J. A.; Afonso, C. N.; Hodgson, E. R. Influence of Defects on the Photoluminescence of Pulsed-Laser Deposited Er-Doped Amorphous Al_2O_3 Films. *Nucl. Instrum. Methods Phys. Res., Sect. B* **2000**, *166*, 793–797.
- (4) Katiyar, P.; Jin, C.; Narayan, R. J. Electrical Properties of Amorphous Aluminum Oxide Thin Films. *Acta Mater.* **2005**, *53*, 2617–2622.
- (5) Mardare, A. I.; Kaltenbrunner, M.; Sariciftci, N. S.; Bauer, S.; Hassel, A. W. Ultra-Thin Anodic Alumina Capacitor Films for Plastic Electronics. *Phys. Status Solidi A* **2012**, *209*, 813–818.
- (6) Vitanov, P.; Harizanova, A.; Ivanova, T.; Dimitrova, T. Chemical Deposition of Al_2O_3 Thin Films on Si Substrates. *Thin Solid Films* **2009**, *S17*, 6327–6330.
- (7) Momida, H.; Hamada, T.; Takagi, Y.; Yamamoto, T.; Uda, T.; Ohno, T. Theoretical Study on Dielectric Response of Amorphous Alumina. *Phys. Rev. B* **2006**, *73*, 054108.
- (8) Farnan, I.; Dupree, R.; Jeong, Y.; Thompson, G. E.; Wood, G. C.; Forty, A. J. Structural Chemistry of Anodic Alumina. *Thin Solid Films* **1989**, *173*, 209–215.
- (9) Kunathfandrei, G.; Bastow, T. J.; Hall, J. S.; Jager, C.; Smith, M. E. Quantification of Aluminum Coordination in Amorphous Aluminas by Combined Central and Satellite Transition Magic-Angle-Spinning NMR-Spectroscopy. *J. Phys. Chem.* **1995**, *99*, 15138–15141.
- (10) Lee, S. K.; Lee, S. B.; Park, S. Y.; Yi, Y. S.; Ahn, C. W. Structure of Amorphous Aluminum Oxide. *Phys. Rev. Lett.* **2009**, *103*, 095501.
- (11) Snijders, P. C.; Jeurgens, L. P. H.; Sloof, W. G. Structural Ordering of Ultra-Thin, Amorphous Aluminium-Oxide Films. *Surf. Sci.* **2005**, *589*, 98–105.
- (12) Oka, Y.; Takahashi, T.; Okada, K.; Iwai, S. I. Structural-Analysis of Anodic Alumina Films. *J. Non-Cryst. Solids* **1979**, *30*, 349–357.
- (13) Lamparter, P.; Kniep, R. Structure of Amorphous Al_2O_3 . *Physica B* **1997**, *234*, 405–406.
- (14) Elmashri, S. M.; Jones, R. G.; Forty, A. J. An Electron-Yield EXAFS Study of Anodic-Oxide and Hydrated-Oxide Films on Pure Aluminum. *Philos. Mag. A* **1983**, *48*, 665–683.
- (15) Gutierrez, G.; Johansson, B. Molecular Dynamics Study of Structural Properties of Amorphous Al_2O_3 . *Phys. Rev. B* **2002**, *65*, 104202.
- (16) Prokhorskii, M. E.; Fofanov, A. D.; Aleshina, L. A.; Nikitina, E. A. Structure of Amorphous Oxide Al_2O_3 : Results of A Molecular-Dynamics Experiment. *Crystallogr. Rep.* **2004**, *49*, 631–634.
- (17) Adiga, S. P.; Zapol, P.; Curtiss, L. A. Atomistic Simulations of Amorphous Alumina Surfaces. *Phys. Rev. B* **2006**, *74*, 064204.
- (18) Lizarraga, R.; Holmstrom, E.; Parker, S. C.; Arrouvel, C. Structural Characterization of Amorphous Alumina and its Polymorphs from First-Principles XPS and NMR Calculations. *Phys. Rev. B* **2011**, *83*, 094201.
- (19) Davis, S.; Gutierrez, G. Structural, Elastic, Vibrational and Electronic Properties of Amorphous Al_2O_3 from Ab Initio Calculations. *J. Phys. Condens. Mater.* **2011**, *23*, 495401.

- (20) Landron, C.; Hennet, L.; Jenkins, T. E.; Greaves, G. N.; Coutures, J. P.; Soper, A. K. Liquid Alumina: Detailed Atomic Coordination Determined from Neutron Diffraction Data Using Empirical Potential Structure Refinement. *Phys. Rev. Lett.* **2001**, *86*, 4839–4842.
- (21) Skinner, L. B.; Barnes, A. C.; Salmon, P. S.; Hennet, L.; Fischer, H. E.; Benmore, C. J.; Kohara, S.; Weber, J. K. R.; Bytchkov, A.; Wilding, M. C.; et al. Joint Diffraction and Modeling Approach to the Structure of Liquid Alumina. *Phys. Rev. B* **2013**, *87*, 024201.
- (22) McHale, J. M.; Auroux, A.; Perrotta, A. J.; Navrotsky, A. Surface Energies and Thermodynamic Phase Stability in Nanocrystalline Aluminas. *Science* **1997**, *277*, 788–791.
- (23) Castro, R. H. R.; Ushakov, S. V.; Gengembre, L.; Gouvea, D.; Navrotsky, A. Surface Energy and Thermodynamic Stability of Gamma-Alumina: Effect of Dopants and Water. *Chem. Mater.* **2006**, *18*, 1867–1872.
- (24) Castro, R. H. R.; Quach, D. V. Analysis of Anhydrous and Hydrated Surface Energies of Gamma-Al₂O₃ by Water Adsorption Microcalorimetry. *J. Phys. Chem. C* **2012**, *116*, 24726–24733.
- (25) Pitcher, M. W.; Ushakov, S. V.; Navrotsky, A.; Woodfield, B. F.; Li, G. S.; Boerio-Goates, J.; Tissue, B. M. Energy Crossovers in Nanocrystalline Zirconia. *J. Am. Ceram. Soc.* **2005**, *88*, 160–167.
- (26) Levchenko, A. A.; Li, G. S.; Boerio-Goates, J.; Woodfield, B. F.; Navrotsky, A. TiO₂ Stability Landscape: Polymorphism, Surface Energy, and Bound Water Energetics. *Chem. Mater.* **2006**, *18*, 6324–6332.
- (27) Navrotsky, A.; Mazeina, L.; Majzlan, J. Size-Driven Structural and Thermodynamic Complexity in Iron Oxides. *Science* **2008**, *319*, 1635–1638.
- (28) Ushakov, S. V.; Navrotsky, A.; Yang, Y.; Stemmer, S.; Kukli, K.; Ritala, M.; Leskela, M. A.; Fejes, P.; Demkov, A.; Wang, C.; et al. Crystallization in Hafnia- and Zirconia-Based Systems. *Phys. Status Solidi B* **2004**, *241*, 2268–2278.
- (29) Eilers, H.; Tissue, B. M. Synthesis of Nanophase ZnO, EU₂O₃, and ZrO₂ by Gas-Phase Condensation With CW-CO₂ Laser-Heating. *Mater. Lett.* **1995**, *24*, 261–265.
- (30) Navrotsky, A. Progress and New Directions in High-Temperature Calorimetry. *Phys. Chem. Miner.* **1977**, *2*, 89–104.
- (31) Navrotsky, A. Progress and New Directions in High Temperature Calorimetry Revisited. *Phys. Chem. Miner.* **1997**, *24*, 222–241.
- (32) Ushakov, S. V.; Navrotsky, A. Direct Measurements of Water Adsorption Enthalpy on Hafnia and Zirconia. *Appl. Phys. Lett.* **2005**, *87*, 164103.
- (33) Saradhi, M. P.; Ushakov, S. V.; Navrotsky, A. Fluorite-Pyrochlore Transformation in Eu₂Zr₂O₇-direct Calorimetric Measurement of Phase Transition, Formation and Surface Enthalpies. *RSC Adv.* **2012**, *2*, 3328–3334.
- (34) Ferreira, A. R.; Kucukbenli, E.; Leitao, A. A.; de Gironcoli, S. Ab Initio Al-27 NMR Chemical Shifts and Quadrupolar Parameters for Al₂O₃ Phases and Their Precursors. *Phys. Rev. B* **2011**, *84*, 235119.
- (35) Chen, S. S.; Avila-Paredes, H. J.; Kim, S.; Zhao, J. F.; Munir, Z. A.; Navrotsky, A. Direct Calorimetric Measurement of Grain Boundary and Surface Enthalpies in Yttria-Stabilized Zirconia. *Phys. Chem. Chem. Phys.* **2009**, *11*, 3039–3042.
- (36) Costa, G. C. C.; Ushakov, S. V.; Castro, R. H. R.; Navrotsky, A.; Muccillo, R. Calorimetric Measurement of Surface and Interface Enthalpies of Yttria-Stabilized Zirconia (YSZ). *Chem. Mater.* **2010**, *22*, 2937–2945.
- (37) Tu, K.-N.; Mayer, J. W.; Feldman, L. C. *Electronic Thin Film Science for Electrical Engineers and Materials Scientists*; McMillan Publishing Company: New York, 1987.
- (38) Kemik, N.; Ushakov, S. V.; Schichtel, N.; Korte, C.; Takamura, Y.; Navrotsky, A. Synthesis and Calorimetric Studies of Oxide Multilayer Systems: Solid oxide Fuel Cell Cathode and Electrolyte Materials. *J. Vac. Sci. Technol., B* **2010**, *28*, CSA1–CSAs.
- (39) *NIST-JANAF Thermochemical Tables*; 4th ed.; Chase, M. W., Ed.; American Institute of Physics and the American Chemical Society: New York, 1998.
- (40) Kemik, N.; Ushakov, S. V.; Gu, M.; Schichtel, N.; Korte, C.; Browning, N. D.; Takamura, Y.; Navrotsky, A. Yttria-Stabilized Zirconia Crystallization in Al₂O₃/YSZ Multilayers. *J. Mater. Res.* **2012**, *27*, 939–943.